Advance Access publication 2024 May 17

Downloaded from https://academic.oup.com/mnras/article/531/2/2642/7676189 by guest on 19 April 2025



A stochastic gravitational wave background in LISA from unresolved white dwarf binaries in the Large Magellanic Cloud

Steven Rieck , 1,2*† Alexander W. Criswell , 1*† Valeriya Korol , 3,4 Michael A. Keim , 5 Malachy Bloom 6 and Vuk Mandic

Accepted 2024 May 10. Received 2024 May 10; in original form 2023 September 2

ABSTRACT

The Laser Interferometer Space Antenna (LISA) is expected to detect a wide variety of gravitational wave sources in the mHz band. Some of these signals will elude individual detection, instead contributing as confusion noise to one of several stochastic gravitational-wave backgrounds (SGWBs) – notably including the 'Galactic foreground', a loud signal resulting from the superposition of millions of unresolved double white dwarf binaries (DWDs) in the Milky Way. It is possible that similar, weaker SGWBs will be detectable from other DWD populations in the local Universe, including the Large Magellanic Cloud (LMC). We use the Bayesian LISA Inference Package (BLIP) to investigate the possibility of an anisotropic SGWB generated by unresolved DWDs in the LMC. To do so, we compute the LMC SGWB from a realistic DWD population generated via binary population synthesis, simulate 4 years of time-domain data with BLIP comprised of stochastic contributions from the LMC SGWB and the LISA detector noise, and analyse this data with BLIP's spherical harmonic anisotropic SGWB search. We also consider the case of spectral separation from the Galactic foreground. We present the results of these analyses and show, for the first time, that the unresolved DWDs in the LMC will comprise a significant SGWB for LISA.

Key words: gravitational waves – white dwarfs – Magellanic Clouds.

1 INTRODUCTION

The launch of the Laser Interferometer Space Antenna (LISA; Amaro-Seoane et al. 2017) in 2035 will revolutionize gravitational wave (GW) astronomy. A space-based gravitational observatory, LISA will detect GWs in the millihertz frequency band, a range inaccessible to both pulsar timing arrays such as the International Pulsar Timing Array (IPTA; Manchester 2013) and current ground-based detector networks such as the Laser Interferometer Gravitational-wave Observatory, the Virgo detector, and the Kamioka Gravitational Wave Detector (KAGRA; Aasi et al. 2015; Acernese et al. 2015; Adhikari et al. 2020).

LISA is expected to detect a wide variety of astrophysical GW sources, including millions of double white dwarfs (DWDs) in the Milky Way (MW) and the nearby Universe (for a review, see Amaro-Seoane et al. 2023). Some of these sources will be individually resolvable, whereas others will contribute to several

potential stochastic gravitational wave backgrounds (SGWBs; e.g. Bonetti & Sesana 2020; Babak et al. 2023; Pozzoli et al. 2023). SGWBs arise from confusion noise formed by the overlap of many unresolved astrophysical or cosmological sources; evidence for such a signal in the nanohertz band has recently been detected (Agazie et al. 2023). While many Galactic DWDs will be individually resolvable by LISA - some serving as verification binaries for the instrument (e.g. Stroeer & Vecchio 2006; Savalle et al. 2022; Finch et al. 2023) – a far greater number of Galactic DWDs will contribute to a stochastic GW signal distributed mostly along the Galactic plane, comprised of the superposition of millions of individually unresolvable DWDs (Edlund et al. 2005). Characterization of this anisotropic MW foreground (so-called due to its prominence above the LISA detector noise) will be necessary in order to subtract it from the LISA data and identify other signals. Additionally, the foreground is of scientific interest in its own right as a means of studying MW structure and star formation history (SFH; e.g. Benacquista & Holley-Bockelmann 2006; Breivik, Mingarelli & Larson 2020; Georgousi et al. 2023).

The MW is not the only host of DWDs detectable with LISA. Recent simulations show that nearby dwarf galaxies including the Large Magellanic Cloud (LMC), Small Magellanic Cloud, and

¹School of Physics and Astronomy, University of Minnesota, Minneapolis, MN 55455, USA

²Department of Physics, University of Cincinnati, Cincinnati, OH 45221, USA

³Max-Planck-Institut für Astrophysik, Karl-Schwarzschild-Straße 1, D-85741 Garching, Germany

⁴Institute for Gravitational Wave Astronomy & School of Physics and Astronomy, University of Birmingham, Birmingham B15 2TT, UK

⁵Department of Astronomy, Yale University, PO Box 208101, New Haven, CT 06520, USA

⁶Department of Physics and Astronomy, Carleton College, Northfield, MN 55057, USA

^{*} E-mail: riecksn@mail.uc.edu (SR); alexander.criswell@ligo.org (AWC) † S. Rieck and A.W. Criswell contributed equally to this work and are co-first authors.

Sagittarius Dwarf contain DWDs that will appear as individually resolvable LISA sources (Roebber et al. 2020a). The number of resolvable DWDs depends on a dwarf galaxy's mass, distance, and SFH (Korol et al. 2020). However, as in the MW, the majority of DWDs in dwarf galaxies will not generate resolvable signals; for instance in the LMC population of $\mathcal{O}(10^6)$ DWDs only $\mathcal{O}(10^2)$ will be individually detectable (Korol et al. 2020). It is possible that, as in the MW, these unresolved DWDs will contribute to an anisotropic SGWB detectable with LISA. To our knowledge, the detectability of SGWBs from nearby dwarf galaxies with LISA anisotropic SGWB searches has not been investigated prior to this work.

Due to its high mass and relative proximity, the LMC is an ideal first candidate to evaluate the possibility of a SGWB from DWDs outside of the MW. Recent work has considered the detectability of individual DWDs in the LMC by constructing model populations based on hydrodynamic simulations and electromagnetic observations of its SFH and stellar density (Keim, Korol & Rossi 2023). Keim et al. found that while the LMC likely has only tens or hundreds of detectable DWDs with LISA signal-to-noise ratio (SNR) >7, it contains approximately two million DWDs in the LISA frequency band. This quantity is significantly less than the DWDs in the MW; the LMC stellar mass (e.g. Marel et al. 2002) is roughly an order of magnitude less than the mass of the MW $(2.7 \times 10^9 \, \mathrm{M}_{\odot})$ versus several $10^{10} \,\mathrm{M}_{\odot}$). At $\sim 50 \,\mathrm{kpc}$ from Earth, the LMC signal is also reduced by distance, as GW amplitudes scale as the inverse of the distance. Given these considerations, we may expect the LMC SGWB to have approximately 1–2 per cent the strength of the MW signal. On the other hand, while the MW DWDs are distributed across a large fraction of the sky, the LMC DWDs are focused in 77 square degrees, making the LMC a good target for an anisotropic SGWB search.

In this work, we simulate and recover the SGWB signal in LISA from a model LMC population using the Bayesian LISA Inference Package (BLIP; Banagiri et al. 2021). In Section 2, we describe the model population used to simulate the LMC signal and our code for simulation and recovery. Results are presented in Section 3 and the conclusions of this study alongside possible future extensions are discussed in Section 4.

2 METHODS

To investigate the stochastic signal from the LMC we use BLIP, described at length in Banagiri et al. (2021). BLIP is a PYTHON package designed for the end-to-end simulation and Bayesian analysis of stochastic GW signals with LISA. In this study, we use the BLIP spherical harmonic anisotropic stochastic search first presented in Banagiri et al. (2021), which is explained in brief in Section 2.1. BLIP can simulate a wide variety of anisotropic stochastic GW signals; we make use of its capability to simulate a SGWB from a realistic simulated population of the unresolved DWDs in the LMC. This population is further described in Section 2.2, while the simulated and recovered models in BLIP are described in Sections 2.3 and 2.4, respectively.

2.1 Anisotropic SGWBs in BLIP

Simulation and recovery of anisotropic SGWBs in BLIP is performed in the spherical harmonic basis. Several studies – considering ground-based, space-based, and pulsar timing-based analyses – have used versions of the spherical harmonic basis for expanding the sky distribution of GW power in e.g. (Ungarelli & Vecchio 2001; Cornish 2001a; Kudoh & Taruya 2005; Taruya & Kudoh 2005; Taruya 2006; Thrane et al. 2009; Mingarelli et al. 2013; Taylor & Gair 2013; Renzini & Contaldi 2018). However, constraining the spherical harmonic distribution to be real and non-negative everywhere is a non-trivial problem that can hamper the accurate characterization of highly anisotropic sources such as the Galactic foreground – or, indeed, the LMC. This is especially true for Bayesian analyses.

Banagiri et al. (2021) developed an explicitly Bayesian version of the spherical harmonic SGWB analysis for LISA wherein this problem was solved by fitting the square root of the GW power. Specifically, the spatial distribution of the SGWB on the sky (for purposes of both simulation and inference) is represented by the spherical harmonic coefficients $b_{\ell m}$. The $b_{\ell m}$ s describe the spherical harmonic expansion of the *square root* of the GW power on the sky $S(\mathbf{n})$. The $b_{\ell m}$ s are related to the usual spherical harmonic coefficients and functions of the GW power on the sky, $a_{\ell m}$ and $Y_{\ell m}$, respectively, via

$$S(\mathbf{n}) = \sqrt{\mathcal{P}(\mathbf{n})} = \left[\sum_{\ell=0}^{\ell_{\max}^a} \sum_{m=-\ell}^{\ell} a_{\ell m} Y_{\ell m}(\mathbf{n}) \right]^{1/2}$$

$$= \sum_{\ell=0}^{\ell_{\max}^b} \sum_{m=-\ell}^{\ell} b_{\ell m} Y_{\ell m}(\mathbf{n}), \qquad (1)$$

where $\ell_{\rm max}^b = \ell_{\rm max}^a/2$ (Banagiri et al. 2021). The $a_{\ell m}$ and $b_{\ell m}$ terms are directly related to each other via simple linear transformations involving Clebsch-Gordan coefficients (Banagiri et al. 2021). Characterizing the GW anisotropy in this way mathematically ensures that the GW power in every proposed sample is real and non-negative across the entire sky (see Banagiri et al. 2021 for details).

In practice, the BLIP anisotropic search infers and produces posterior distributions for each $b_{\ell m}$ coefficient (alongside spectral parameters; see Section 2.4) up to some $\ell_{\max}^b = \ell_{\max}^a/2$. Using a higher ℓ_{\max}^a for the anisotropic search increases the angular resolution of the search, but also increases the number of parameters that one must infer as $N_{\text{par,sph}} \propto \ell_{\max}^a (\ell_{\max}^a + 1)/2$. Additionally, as the BLIP anisotropic search considers the LISA detector response to each spherical harmonic, the computational resources required to analyse data at large ℓ_{\max}^a can become limiting.

This latter point is also a limitation for simulation of anisotropic SGWBs with BLIP, as the SGWB spatial distribution is simulated in the spherical harmonic basis. Accordingly, simulations of anisotropic signals in BLIP similarly employ a truncation ℓ_{\max}^a . This, of course, results in highly-localized signals (like the LMC) spreading out over an area much larger than their true spatial extent on the sky. However, a study of BLIP's angular resolution (Bloom et al., in-prep) has shown that the value of ℓ_{\max}^a used in the SGWB simulation does not impact the final spatial recovery so long as $\ell_{\max,\text{simulation}}^a \geq \ell_{\max,\text{recovery}}^a$. (Simply put, our analysis is insensitive to variations on smaller scales than it parametrizes, as one would expect intuitively.) Development work is ongoing to improve BLIP's performance for both simulation

 $^{^{1}}$ The LMC is expected to contain approximately 61 million DWDs in total, but a vast majority are non-interacting with large orbital separations and are negligible sources of GWs. A frequency cut-off of 10^{-4} Hz reduces this number to two million in the LISA frequency band (Keim et al. (2023), by correspondence with the author).

²As the usual spherical harmonic ℓ_{\max} referred to in the literature is ℓ_{\max}^a , we will quote this truncation ℓ_{\max} in terms of ℓ_{\max}^a throughout this work.

and analysis at high ℓ_{\max}^a (\gtrsim 8), but these computational limitations remain relevant at present.

2.2 Simulated LMC DWD population

To date, no DWD has been observed in the LMC. Even within the MW most of the known LISA-detectable DWDs are found within a few kpc (e.g. Kupfer et al. 2024); this is mainly due to the faint nature of white dwarf stars. Nonetheless, this highlights an opportunity for LISA to reveal the DWD population inaccessible to electromagnetic observatories as far as the LMC. To model the LMC DWDs we employ a mock catalogue compiled by Keim et al. (2023). It is based on a fiducial DWD population synthesis model computed with the SEBA code (Portegies Zwart & Verbunt 1996; Toonen, Nelemans & Portegies Zwart 2012), which has been calibrated on the observed DWDs (albeit in the Solar neighbourhood) and, therefore, is in good agreement with the observed DWD space density and mass-ratio distribution (Toonen et al. 2012, 2017).

Synthetic DWDs are distributed across the sky and assigned formation times and ages based on the Magellanic Clouds Photometric Survey and the observed, spatially resolved 2D SFH from Harris & Zaritsky (2009, for a visual representation see their fig. 4). We refer to Keim et al. (2023, see their 'Model 1') for further details.

For the assumed LMC total stellar mass of $2.7 \times 10^9 \,\mathrm{M}_{\odot}$ (van der Marel et al. 2002), the adopted model yields $\sim 2 \times 10^6$ DWDs in the LISA frequency band. For this model, only about \sim 500 DWD are individually resolved with SNR >7, assuming the mission lifetime of 4 yr with 100 per cent duty cycle. The detectable binaries have frequencies >1.7 mHz (or equivalently binary orbital periods of <20 min) due to LISA's selection effects. The total number of LISA sources in the LMC represents about 8 per cent of the MW DWD population. As detailed in Keim et al. (2023), the difference between the two populations is twofold. Firstly, the number of LISA sources (and stars in general) scales linearly with the total mass of the host galaxy. The lower mass of the LMC thus decreases individual DWD detections. Secondly, unlike the MW, the LMC is an active site of star formation, and so a significant fraction of DWD in the adopted model have formed only $\sim \mathcal{O}(10^2)$ Myr ago. This active star formation increases detections of individual DWDs in the LMC.

2.3 Simulated LISA Data

The simulation of stochastic GW signals from DWD populationsynthesis catalogues is a novel BLIP feature demonstrated for the first time in this work. For each catalogue binary, we compute the (assumed monochromatic) strain amplitude from its binary masses and orbital frequency, following the conventions in Wagg, Breivik & de Mink (2022). We use the catalogue sky position and distance (as seen in the Solar system Barycentre frame) to bin the population in both frequency and sky direction. Binning on the sky is performed on a HEALPIX (Gorski et al. 2005) map, with user-specified skymap pixel resolution, quantified by the HEALPIX nside. In this work, we use an nside of 8 to generate our simulated signal. At our chosen skymap resolution, the area of each pixel equals approximately 53 square degrees. The angular size of the LMC is approximately 77 square degrees (Roebber et al. 2020b). Thus, in our initial simulated skymap the entire LMC is contained within only a few pixels. Simulating the LMC with a higher nside would incur significantly higher computational cost for little-to-no ultimate effect due to limitations on the sky resolution of our analysis (see Section 2.1).

To compute the associated SGWB spectrum of the DWD population, we assume all DWD systems with individual SNR >7 are

individually resolvable and can be subtracted from the data (Keim et al. 2023). We use LEGWORK (Wagg et al. 2022) to calculate the SNR of every DWD considering the instrumental noise and MW foreground given in Robson, Cornish & Liu (2019), and remove from the population those DWDs with SNR >7. Disentangling the resolved and unresolved DWDs - let alone the entire cacophony of LISA sources - is beyond the scope of this work, requiring a global, simultaneous solution (e.g. Littenberg & Cornish 2023). We assume all other GW sources are perfectly characterized and subtracted from the data, and we first simulate a signal that includes only the unresolved LMC DWDs. In a second analysis, we also include a simple model of the MW foreground (see Section 2.3). Our simulation of the LMC DWDs is identical in each analysis. The monochromatic strains of the remaining unresolved binaries are then binned in frequency at a frequency resolution determined by the LISA nominal mission duration of 4 years, i.e. $\Delta f = 1/T_{\rm obs} \simeq$ 8×10^{-9} Hz. We consider a frequency range of $f \in [10^{-4}, 10^{-2}]$ Hz, as this will be the most-sensitive band of the LISA detector.

After the population skymap and spectrum are computed, BLIP simulates a time series of the corresponding stochastic signal. It does so by computing the spherical harmonic representation of the population skymap up to some $\ell_{\rm max}^a$ (we consider a simulation $\ell_{\rm max}^a$ of 4 due to computational limitations; see Section 2.1). BLIP convolves both this spherical harmonic expansion and the population spectrum with the time-varying LISA response across frequency and all considered spherical harmonic modes (see Banagiri et al. 2021 for details). Note that this process explicitly models the orbits of the LISA constellation and as such naturally accounts for the time-varying amplitude of highly anisotropic SGWBs like that of the LMC and the MW. The simulated population skymap as represented in the spherical harmonic basis can be found in Fig. 1(a).

The resulting GW time series is added to Gaussian detector noise with the spectral form given in the LISA proposal (Amaro-Seoane et al. 2017), reproduced below in equations (2) and (3), with $N_p = 9 \times 10^{-42}$ and $N_a = 3.6 \times 10^{-49} \, \mathrm{Hz^{-4}}$ for the position and acceleration noise contributions, respectively:

$$S_{p}(f) = N_{p} \left[1 + \left(\frac{2mHz}{f} \right)^{4} \right] Hz^{-1}, \tag{2}$$

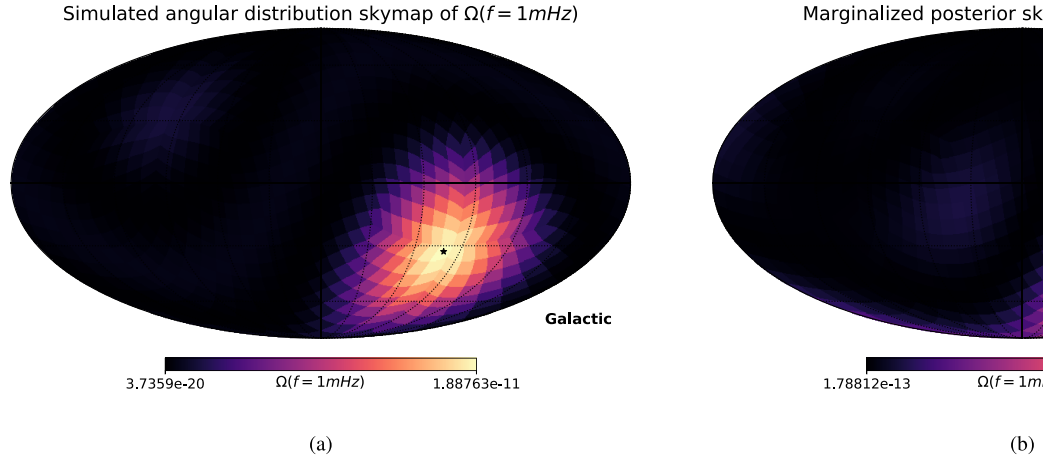
$$S_{a}(f) = \left[1 + \left(\frac{0.4mHz}{f} \right)^{2} \right] \left[1 + \left(\frac{f}{8mHz} \right)^{4} \right]$$

$$\times \frac{N_{a}}{(2\pi f)^{4}} Hz^{-1}. \tag{3}$$

Throughout this study we simulate and model LISA data using the X—Y—Z time-delay interferometry (TDI) channels (see Tinto & Dhurandhar (2014) for a review of TDI in LISA). For further details on the BLIP data simulation procedure, see Banagiri et al. (2021). The simulated spectrum, as it appears in the detector, along with the simulated detector noise, is included in Fig. 3.

2.3.1 Simple MW foreground

We also include a simple analytic (i.e. non-population) simulation of the MW foreground. Its spatial distribution follows the simple bulge + disc model described in Breivik et al. (2020). We use the 'thin' model (see Breivik et al. (2020) for details), with radial scale height $r_{\rm h}=2.9$ kpc and vertical scale height $z_{\rm h}=0.3$ kpc. This simulated Galaxy is then used to create a skymap in the Solar System Barycentre frame as described in section 6 of Banagiri et al. (2021). As throughout the rest of this work, we represent this spatial



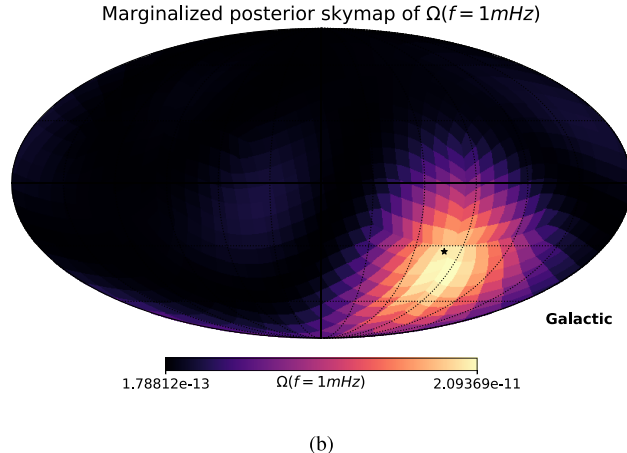


Figure 1. (a) The simulated sky distribution of $\Omega_{GW}(1\text{mHz})$ for the LMC SGWB generated by our model DWD population. (b) The marginalized posterior sky distribution of $\Omega_{GW}(1\text{mHz})$ inferred by our analysis of the LMC in isolation. Both skymaps are in the spherical harmonic basis at $\ell_{\max}^a = 4$ and display distribution of the dimensionless GW energy density Ω_{GW} evaluated at 1 mHz. These skymaps do not include LISA instrumental noise. The black star marks the position of the LMC. The recovered sky distribution is consistent with both the simulated sky distribution and the position of the LMC.

distribution in the spherical harmonic basis. For the MW foreground spectrum, we use a tanh-truncated power law similar to that of (e.g.) Robson et al. (2019), such that

$$\Omega(f) = \Omega_{\text{ref}} \left(\frac{f}{f_{\text{ref}}} \right)^{\alpha} \left(1 + \tanh \left(\frac{f_{\text{cut}} - f}{f_{\text{scale}}} \right) \right), \tag{4}$$

where for this simulation $\Omega_{\rm ref} = 2 \times 10^{-5}$, $f_{\rm ref} = 25$ Hz, $f_{\rm cut} = 2$ mHz, and $f_{\text{scale}} = 0.4$ mHz. Although this more simplistic analytic function does not account for iterative subtraction of resolved MW DWDs, it remains a sufficient approximation for our purposes given the large uncertainties in the overall amplitude and shape of the MW foreground signal. This skymap and spectrum are then used to compute the GW time-series contribution of the MW foreground in the same manner as described above for the LMC.

2.4 Model recovery in BLIP

After generating the simulated data, BLIP performs Bayesian parameter estimation via nested sampling with DYNESTY (Speagle 2020). This process is described in brief below; reference Banagiri et al. (2021) for a more detailed treatment. The BLIP anisotropic search simultaneously models the LISA detector noise, the SGWB spectral distribution, and the SGWB spatial distribution, inferring posterior distributions for each of the parameters described below.

LISA's instrumental noise is modelled in terms of the position and acceleration noise amplitudes N_p and N_a , with the spectral form given by equations (2) and (3). We characterize the LMC SGWB spectrum using a power-law spectral model of the form

$$\Omega(f) = \Omega_{\text{ref}} \left(\frac{f}{f_{\text{rof}}} \right)^{\alpha}, \tag{5}$$

where $\Omega_{\rm ref} = \Omega(f_{\rm ref} = 25\,{\rm Hz})$ is the power-law amplitude at the reference frequency f_{ref} and α is the power-law spectral index (slope). The value of $f_{\rm ref}$ is an arbitrary choice. BLIP recovers both $\Omega_{\rm ref}$ and α as free parameters. The majority of the LMC SGWB spectrum can be approximated as a power law, although this model will be unable to capture the high-frequency turnover in the spectrum; as this work focuses on establishing the LMC SGWB as a significant signal in LISA, more complex spectral models are left to future work (see Section 4).

As discussed in Section 2.1, the spatial distribution of the LMC SGWB on the sky is inferred in the spherical harmonic basis. Our final spatial posteriors are given in terms of the $b_{\ell m}$ s, from which it is straightforward to compute the corresponding $a_{\ell m}$ s and SGWB power skymap. We choose an analysis ℓ_{\max}^a of 4, in keeping with our choice for the simulated LMC spatial distribution.

The Fourier-domain likelihood used in BLIP's nested sampling is a complex multivariate Gaussian (Adams & Cornish 2010) whose covariance is a function of the parameters in the previous four equations: $\mathcal{L}(\tilde{d}|N_p, N_a, \Omega_{\text{ref}}, \alpha, \{b_{\ell,m}\})$. The likelihood is given by equation 32 from Banagiri et al. (2021):

$$\mathcal{L}(\tilde{d}|N_{p}, N_{a}, \Omega_{\text{ref}}, \alpha, \{b_{\ell,m}\}) = \prod_{f,t} \frac{1}{2\pi T_{\text{seg}} |\mathbf{C}_{IJ}(f, t)|} \times \exp\left(-\frac{2\tilde{d}_{f,t}^{*} \mathbf{C}_{IJ}(f, t)^{-1} \tilde{d}_{f,t}}{T_{\text{seg}}}\right)$$
(6)

where T_{seg} is the length of each time segment, $C_{\text{IJ}}(f, t)$ is the channel covariance matrix, and $\tilde{d}_{f,t}$ is the array of data in the Fourier domain for the three LISA channels measured in the time segment labelled by t and at frequency f. For explicit definitions of these terms see discussion in Banagiri et al. (2021) and original derivations in Cornish & Larson (2001) and Cornish (2001b).

2.4.1 Joint model with the MW foreground

We also consider a joint model that simultaneously infers the LMC SGWB alongside the MW foreground. This is a simplified, prototype demonstration of the full, flexible spectral separation infrastructure developed for BLIP (Criswell et al. in preparation). Accordingly, we restrict ourselves to a simple MW model: we assume the MW spatial distribution is well-measured a priori from the resolved Galactic DWDs, and fix its skymap to the analytic distribution described in Section 2.3. We then use the spectral model of equation (4), fixing $f_{\text{scale}} = 0.4 \text{ mHz}$, and inferring the set of free parameters $\theta_{MW} = \{\Omega_{ref,MW}, \alpha_{MW}, f_{cut}\}$. The joint likelihood is then $\mathcal{L}(d|\theta_n;\theta_{LMC};\theta_{MW})$, where $\theta_n = \{N_p, N_a\}$ describe the noise and $\theta_{\text{LMC}} = \{\Omega_{\text{ref}}, \alpha, \{b_{\ell,m}\}\}\$ describe the LMC as discussed above. We leave a full discussion of BLIP's approach to spectral separation to Criswell et al. (in preparation). We stress that this simple model is a first pass at resolving the LMC SGWB in the presence of the MW

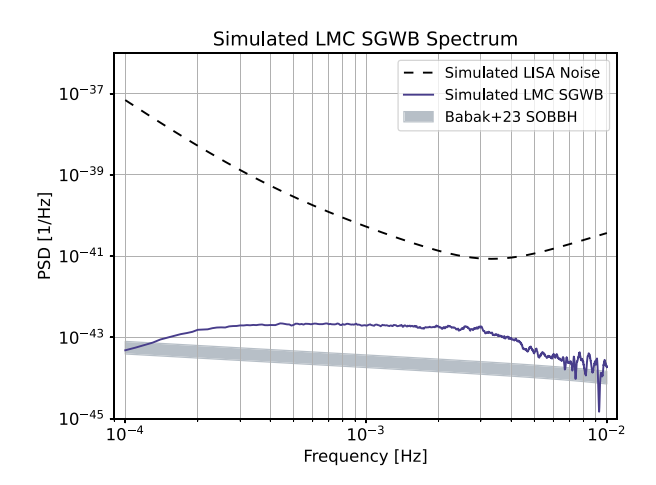


Figure 2. The simulated, population-derived LMC SGWB power spectral density (PSD). The LISA instrumental noise spectrum and the Babak et al. (2023) interquartile prediction for the LISA SOBBH SGWB are shown for reference. Both SGWB PSDs are shown convolved with the LISA response. Note that the LMC SGWB amplitude exceeds that of the SOBBH signal in the relevant frequency band.

foreground. A detailed treatment of spectral separation between the LMC and MW signals is sufficiently involved so as to warrant its own dedicated study.³ As such, more complicated models are outside the scope of this initial work, which primarily seeks to establish the LMC SGWB as a significant stochastic contribution in LISA.

3 RESULTS

We include results from two simulations. In the first, we simulate the LMC SGWB generated from the population described in Section 2.2 with LISA instrumental noise. In Section 3.2, we present the results of the recovery process described in Section 2.4. In Section 3.3, we present a recovery of the LMC in the presence of a simple realization of the MW foreground, as described in Section 2.4.1.

3.1 LMC SGWB spectrum

The population-derived power spectrum of the LMC SGWB is shown in Fig. 2. Notably, the amplitude of the LMC signal is comparable to – and even exceeds – that of the expected SGWB from extragalactic stellar-origin binary black holes (SOBBHs), shown here using the observationally driven estimate of Babak et al. (2023). The LMC signal will therefore comprise a significant SGWB for LISA, and will be important to consider in efforts to characterize the SOBBH SGWB and other underlying SGWBs. This result is the first demonstration of the LMC SGWB as a relevant signal for LISA.

3.2 Recovery of the LMC SGWB in isolation

We present here an analysis of the LMC SGWB in isolation (i.e. assuming the MW foreground has been subtracted) using an integration time of 1.26×10^8 s, approximately the planned LISA mission duration of 4 years, and considering a frequency band of $f \in [10^{-4}, 10^{-2}]$ Hz. We simulate and recover the LMC SGWB in the spherical harmonic basis, use a power law to model the SGWB spectrum, and model the LISA detector noise according to the spectral form given

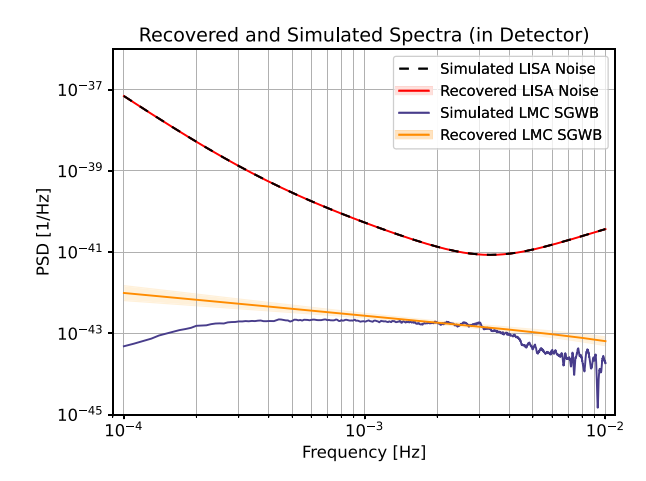


Figure 3. The simulated and inferred PSD of the LMC SGWB and the LISA detector noise. For the inferred spectra, the solid lines and shaded regions are the median and 95 per cent credible intervals, respectively, of the marginalized posterior spectral fit. As can be seen in Fig. A1, the noise spectrum is recovered extremely precisely; as a result the 95 per cent credible intervals are difficult to see by eye. Note that the power-law spectral fit has highest fidelity to the simulated LMC spectrum over the sensitive band of 1–4 mHz.

in equations (2) and (3). The corresponding marginalized posterior skymap computed from the inferred $b_{\ell m}$ s is shown in Fig. 1(b), and the marginalized posterior detector-convolved power spectral density (PSD) is shown in Fig. 3 (alongside the PSDs of the simulated detector noise and of the SGWB due to the LMC DWD population). Posterior samples for all parameters are shown in Fig. A1.

As seen in Fig. 1(b), the inferred distribution of power on the sky is consistent with both the true position of the LMC and the simulated LMC SGWB skymap (Fig. 1a). While more precise localization of the LMC SGWB could in principle be achieved with higher ℓ_{\max}^a or a targeted directional search that takes advantage of the known position of the LMC, we leave these avenues of exploration to future work.

The inferred power-law spectrum of the LMC SGWB is shown in Fig. 3, alongside the simulated and inferred noise spectra and the simulated population-derived spectrum of the LMC SGWB. The inferred amplitude and slope of the power-law model used in this study are most impacted by the shape of the LMC spectrum at frequencies where its SNR is largest - namely 1-4 mHz, where the simulated LMC spectrum is closest to the LISA noise curve. At frequencies outside this range, the power-law model does not adequately describe the complexity of the simulated LMC SGWB spectrum, and hence it overestimates the contribution from the LMC signal at these frequencies. We leave treatment of more complex or non-parametric spectral models to future work, although we note that the overall low SNR of the LMC may make constraining highlycomplex models difficult (unless the dimensionality of the inference problem is otherwise reduced by, for example, a targeted directional search). The noise spectra is recovered extremely well, due to the fact that we recover it using the exact functional form that we initially simulate. Ultimately the noise spectral shape will not be precisely known, which will introduce additional error.

Finally, we perform model comparison via Bayes factor and consider two cases: our power-law spherical harmonic model including LISA noise and the LMC SGWB, and a noise-only model. Using the same four-year data set including the LMC SGWB described in Section 2.3, we repeat our analysis using a model that only accounts

³See Section 4 for further discussion as to what such a study could entail.

for the LISA detector noise in terms of N_p and N_a as given in equations (2) and (3) (neglecting the presence of any kind of underlying SGWB). Computing the Bayesian evidences of each model (\mathcal{Z}_1 for the noise + SGWB model; \mathcal{Z}_2 for the noise-only model) is trivial due to our use of nested sampling via DYNESTY, which produces the Bayesian evidence as its primary product (Speagle 2020). We compute the log Bayes factor to be

$$\log K = \log \mathcal{Z}_1 - \log \mathcal{Z}_2 = 310 \pm 3,$$

constituting decisive evidence⁴ in favour of our SGWB plus noise model over the noise-only model. We conclude that – in the absence of the MW foreground signal and for the case of stationary, Gaussian noise with a fixed, equilateral LISA constellation – we are able to detect and characterize the LMC SGWB signal. Relaxing any of these assumptions will reduce LISA's sensitivity to SGWBs (see e.g. Hartwig et al. 2023; Muratore, Gair & Speri 2024) and, accordingly, impact the ability of the LISA to detect and characterize the LMC SGWB. While fully accounting for these factors is beyond the scope of this work, we present a simplified treatment of a search for the LMC SGWB in the presence of the MW foreground in the following section.

3.3 Recovery of the LMC SGWB with the MW foreground

We now turn to the case of the LMC SGWB in the presence of the MW foreground. We additionally include in our simulated data a simple MW foreground as described in Section 2.3; the simulation procedure for the LISA instrumental noise and LMC SGWB is otherwise unchanged. This new data set is then analysed with the joint inference model described in Section 2.4.1; all other quantities of interest (integration time, frequency range, etc.) are identical to the procedure described in Section 3.2 for the LMC in isolation. We find that, despite the presence of the MW foreground, we are again able to detect and characterize the simulated LMC SGWB. The recovered spectral distribution of the LMC SGWB in the presence of the MW foreground is shown in Fig. 4, alongside those of the noise and the MW foreground. As before, we display the simulated and inferred spectra for each of our model components. Our recovered model successfully describes the LISA instrumental noise, MW foreground, and LMC SGWB simultaneously. Posterior samples for all spectral parameters are shown in Fig. A2. The presence of the MW does affect the recovered LMC SGWB, reducing the recovery quality below \sim 3 mHz causing the power law to even more dramatically overestimate the LMC SGWB. Above \sim 3 mHz, the recovered power law follows closely above the simulated LMC SGWB spectrum. It is again clear that the majority of information is being gleaned from the region around \sim 3 mHz where the LMC SNR would be highest; more refined spectral models may be able to leverage this fact in future.

The LMC SGWB spatial recovery in the presence of the MW foreground can be seen in Fig. 5. It is important to note that this figure only displays the inferred distribution of power on the sky (i.e. the spherical harmonic spatial model for the LMC SGWB), and does not include the contribution from the MW (which is assumed known and therefore not inferred; see Section 2.4.1). The associated posterior samples are shown in Fig. A3. As would be expected, the quality of the spatial recovery is degraded somewhat in the presence of the MW (and with a more statistically complex signal model).

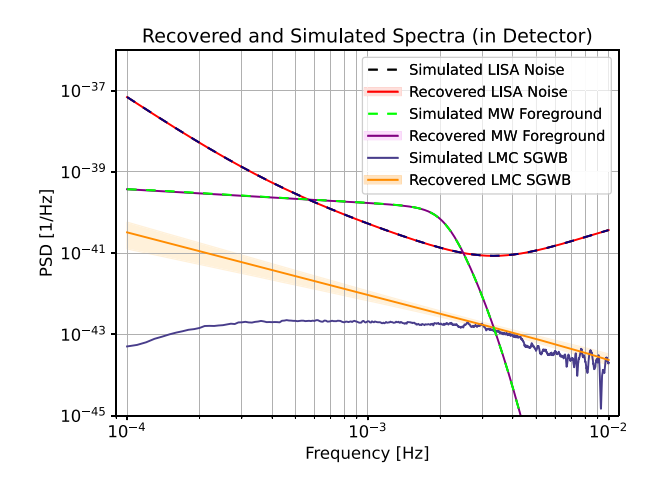


Figure 4. The simulated and inferred PSDs of the LMC SGWB, the MW foreground, and the LISA detector noise. For the inferred spectra, the solid lines and shaded regions are the median and 95 per cent credible intervals, respectively, of the marginalized posterior spectral fit. The precise recovery of both the LISA noise and MW foreground renders their respective medians and 95 per cent credible intervals nearly indistinguishable. The simple power-law model for the LMC signal again results in an overestimation of power at low frequencies. The signal is most accurately recovered above 3 mHz where the contribution from the MW foreground is minimal.

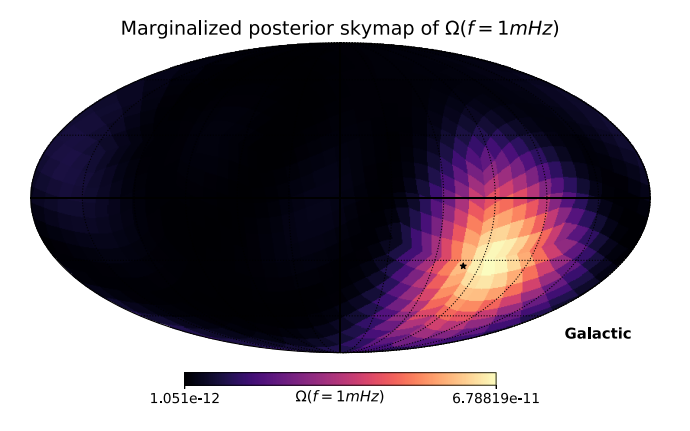


Figure 5. The marginalized posterior sky distribution of $\Omega_{GW}(1 mHz)$ inferred by our analysis for the LMC SGWB in the presence of the MW foreground. The simulated LMC in this simulation is identical to Fig. 1(a). We represent the signal in the spherical harmonic basis at $\ell_{max}^a = 4$. This skymap does not include LISA instrumental noise or the MW foreground, though both are present in the simulation. The black star marks the true position of the LMC. The recovered sky distribution is consistent with both the simulated signal and the true position of the LMC.

While the extent of the inferred LMC spatial distribution is similar to the simulated skymap and the true position of the LMC is included in our recovered spatial distribution, it does experience some bias, shifting slightly off of the true position of the LMC.

Finally, we again perform a second analysis of the same simulated LISA data (including LISA instrumental noise, the MW foreground, and the LMC SGWB) with a model which accounts for LISA instrumental noise and the MW foreground, but neglects the presence of the LMC. We compute the log Bayes factor ($\log K$) for this case using the Bayesian evidences of each model (\mathcal{Z}_1 for the LMC-included model; \mathcal{Z}_2 for the LMC-absent model):

$$\log K = \log \mathcal{Z}_1 - \log \mathcal{Z}_2 = 92 \pm 4,$$

⁴For reference, a log Bayes factor of 1 is substantial to strong evidence, and any log Bayes factor >2 is typically considered decisive evidence in favour of one model over another (Kass & Raftery 1995).

While this Bayes factor is reduced compared to that for the LMC in isolation – as expected, the MW foreground makes the LMC SGWB more difficult to recover – it still constitutes extremely decisive evidence in favour of the model that includes the LMC SGWB.

4 DISCUSSION AND CONCLUSIONS

In this work, we evaluate for the first time the existence and prospects for LISA of an anisotropic SGWB arising from the unresolved DWDs in the LMC. We use a population catalogue generated using realistic stellar synthesis codes to create a model of the LMC, which we then use to simulate its DWD-generated SGWB with BLIP. We use BLIP's spherical harmonic, Bayesian search for anisotropic SGWBs to demonstrate a proof-of-concept recovery of the LMC SGWB both in isolation and in the presence of the MW foreground.

We find that the simulated SGWB from the unresolved DWDs in the LMC can be recovered in the presence of LISA instrumental noise using BLIP with 4 years of integration time and a power-law spherical harmonic signal model. Model comparison between the noise + SGWB power-law spherical harmonic model and a noise-only model yields decisive evidence in favour of the presence of the LMC SGWB signal. The recovered position of the LMC on the sky is consistent with its true location, and the LMC SGWB spectrum can be well modelled as a simple power law over the sensitive frequency band (roughly 1–4 mHz).

Additionally, we find that we are able to simultaneously recover the LMC SGWB and a rudimentary model of the MW foreground. While the presence of the MW has a noticeable, adverse effect on the recovery of the LMC SGWB, the recovered spatial distribution remains consistent with the true position of the LMC, and our power-law spectral model only slightly overestimates the LMC spectrum above 3 mHz. As in the LMC-only case, model comparison via Bayes factor yields decisive evidence in favour of the presence of the LMC SGWB signal. While a detailed treatment of spectral separation between realistic, population-derived realizations of the MW and LMC signals is required to make a strong statement of detectability – and remains a subject of future work – this result is none the less extremely promising for the prospects of LISA to detect and characterize the LMC SGWB.

While the power-law spectral model employed here is accurate to the simulated LMC spectrum where the LISA noise curve is lowest and the MW foreground has dropped off, outside these areas, it does not capture the full spectral shape of the LMC SGWB. Further characterization of the LMC SGWB with more complex spectral and/or spatial models is one promising avenue of future work. One could, for example, leverage the known location of the LMC to infer only its spectral distribution while holding its spatial distribution fixed, thereby reducing model complexity along one axis and allowing for (e.g.) a truncated or broken power-law spectral model to better capture the cut-off in the LMC SGWB spectrum. Such a model could also be informed by our theoretical knowledge of the LMC SGWB, either by setting astrophysically motivated priors on its parameters, or fixing those parameters that see little variation across different population-synthesis realizations of the LMC. Conversely, ongoing efforts to incorporate non-parametric spectral models into BLIP could enable more accurate characterization of the LMC spectrum, at the cost of increased difficulty of spectral separation from the MW foreground. With more precise spectral models, it may be possible to characterize the LMC SGWB well enough to gain information about the distribution of DWDs in the LMC and learn about its structure, mass, and/or SFH. Methods have been proposed to study the MW in this way using the unresolved Galactic DWDs (e.g. Breivik et al. 2020), so it is possible that similar techniques could be used to study the LMC. In particular, it may be possible to achieve a measurement of the LMC mass via a similar approach to the one described in Korol et al. (2021), which used the resolvable binaries in the LMC. Additionally, the analysis presented in this work is generalizable to simulation and recovery of the (albeit weaker) SGWBs from the Small Magellanic Cloud and other dwarf galaxy satellites of the MW.

Finally, the development of refined approaches to concurrent characterization of the LMC SGWB and the MW foreground will be vital moving forward. The spectral overlap between these signals is significant; neglecting to properly account for the LMC SGWB could lead to spectral biases for analyses of the MW foreground. Despite their close proximity in terms of LISA's angular resolution, the spatial distributions of the MW and LMC are distinct on the sky and – as demonstrated in this work – can be used to aid in spectral separation between these signals. In particular, the spatial distribution of the LMC on the sky is well known from electromagnetic observations; our anisotropic search at high ℓ_{\max}^a and/or a targeted directional search could leverage this fact. One could also incorporate concurrent GW localization measurements of the resolved DWDs in the LMC, improving prospects for resolving the LMC SGWB by jointly modelling the 3D spatial distribution of the LMC population (as has been proposed for the MW population; Adams, Cornish & Littenberg 2012). Finally, a pixel-basis method to describe the spatial distribution of a signal provides a promising alternative to a sphericalharmonic basis approach, which by necessity describes the entire sky rather than the region containing the LMC specifically. This method would be well suited to enabling realistic spectral separation of the stochastic contributions from unresolved MW and LMC

Proper, joint treatment of both the LMC SGWB and MW foreground will likely be crucial for detecting and characterizing other, lower amplitude SGWBs. The SOBBH background (e.g. Babak et al. 2023) is likely of comparable or lower amplitude in comparison to the LMC SGWB (see Fig. 2). Characterization of the LMC SGWB is thus extremely relevant when considering the search for the SOBBH SGWB, as well as other, underlying backgrounds – including those of cosmological origin.

ACKNOWLEDGEMENTS

This work is supported by the National Aeronautics and Space Administration grant 90NSSC19K0318, and utilized computing resources provided by the Minnesota Supercomputing Institute at the University of Minnesota. Packages used for this work include NUMPY (Harris et al. 2020), SCIPY (Virtanen et al. 2020), CHAINCONSUMER (Hinton 2016), and MATPLOTLIB (Hunter 2007). The authors would like to thank Sharan Banagiri, Joe Romano, and Jessica Lawrence for their work on BLIP and many helpful conversations, as well as the anonymous reviewer for their thorough and insightful comments and suggestions.

DATA AVAILABILITY

All data and code used in this study is publicly available. The simulated LMC population data along with all generated SGWB data and resulting posterior distributions are available at https://zenodo.org/records/10783952. The BLIP package is open source and is available at https://github.com/sharanbngr/blip.

Littenberg T. B., Cornish N. J., 2023, Phys. Rev. D, 107, 063004

Muratore M., Gair J., Speri L., 2024, Phys. Rev. D, 109, 042001

Portegies Zwart S. F., Verbunt F., 1996, A&A, 309, 179

Renzini A., Contaldi C., 2018, MNRAS, 481, 4650

Marel R. P. v. d., Alves D. R., Hardy E., Suntzeff N. B., 2002, AJ, 124, 2639

Mingarelli C. M. F., Sidery T., Mandel I., Vecchio A., 2013, Phys. Rev. D,

Pozzoli F., Babak S., Sesana A., Bonetti M., Karnesis N., 2023, Phys. Rev.

Manchester R. N., 2013, Class. Quantum Gravity, 30, 224010

Kupfer T. et al., 2024, ApJ, 963, 100

88, 062005

D. 108, 103039

REFERENCES

L55

Aasi a. J. et al., 2015, Class. Quantum Gravity, 32, 074001 Acernese F. et al., 2015, Class. Quantum Gravity, 32, 024001 Adams M. R., Cornish N. J., 2010, Phys. Rev. D, 82, 022002 Adams M. R., Cornish N. J., Littenberg T. B., 2012, Phys. Rev. D, 86, 124032 Adhikari R. X. et al., 2020, Class. Quantum Gravity, 37, 165003 Agazie G. et al., 2023, ApJ, 951, L8 Amaro-Seoane P. et al., 2017, Laser Interferometer Space Antenna, https: //arxiv.org/abs/1702.00786 Amaro-Seoane P. et al., 2023, Living Reviews in Relativity, 26, 2 Babak S. et al., 2023, Journal of Cosmology and Astroparticle Physics, 034 Banagiri S., Criswell A., Kuan T., Mandic V., Romano J. D., Taylor S. R., 2021, MNRAS, 507, 5451 Benacquista M., Holley-Bockelmann K., 2006, ApJ, 645, 589 Bonetti M., Sesana A., 2020, Phys. Rev. D, 102, 103023 Breivik K., Mingarelli C. M. F., Larson S. L., 2020, ApJ, 901, 4 Cornish N. J., 2001a, Class. Quant. Grav., 18, 4277 Cornish N. J., 2001b, Phys. Rev. D, 65, 022004 Cornish N. J., Larson S. L., 2001, Class. Quantum Gravity, 18, 3473 Edlund J. A., Tinto M., Krolak A., Nelemans G., 2005, Phys. Rev. D, 71, 122003 Finch E. et al., 2023, mnras, 522, 5358 Georgousi M., Karnesis N., Korol V., Pieroni M., Stergioulas N., 2023, MNRAS, 519, 2552 Gorski K. M., Hivon E., Banday A. J., Wandelt B. D., Hansen F. K., Reinecke M., Bartelman M., 2005, ApJ, 622, 759 Harris J., Zaritsky D., 2009, AJ, 138, 1243 Harris C. R. et al., 2020, Nature, 585, 357 Hartwig O., Lilley M., Muratore M., Pieroni M., 2023, Phys. Rev. D, 107, 123531 Hinton S. R., 2016, J. Open Source Softw., 1, 00045 Hunter J. D., 2007, Comput. Sci. Eng., 9, 90 Kass R. E., Raftery A. E., 1995, J. Am. Stat. Assoc., 90, 773 Keim M. A., Korol V., Rossi E. M., 2023, MNRAS, 521, 1088 Korol V. et al., 2020, A&A, 638, A153 Korol V., Belokurov V., Moore C. J., Toonen S., 2021, MNRAS, 502,

Kudoh H., Taruya A., 2005, Phys. Rev. D, 71, 024025

Robson T., Cornish N. J., Liu C., 2019, Class. Quantum Gravity, 36, 105011 Roebber E. et al., 2020a, ApJ, 894, L15 Roebber E. et al., 2020b, ApJ, 894, L15 Savalle E., Gair J., Speri L., Babak S., 2022, Phys. Rev. D, 106, 022003 Speagle J. S., 2020, MNRAS, 493, 3132 Stroeer A., Vecchio A., 2006, Class. Quant. Grav., 23, S809 Taruya A., 2006, Phys. Rev. D, 74, 104022 Taruya A., Kudoh H., 2005, Phys. Rev. D, 72, 104015 Taylor S. R., Gair J. R., 2013, Phys. Rev. D, 88, 084001 Thrane E., Ballmer S., Romano J. D., Mitra S., Talukder D., Bose S., Mandic V., 2009, Phys. Rev. D, 80, 122002 Tinto M., Dhurandhar S. V., 2014, Living Rev. Rel., 17, 6 Toonen S., Nelemans G., Portegies Zwart S., 2012, A&A, 546, A70 Toonen S., Hollands M., Gänsicke B. T., Boekholt T., 2017, A&A, 602, A16 Ungarelli C., Vecchio A., 2001, Phys. Rev. D, 64, 121501 Virtanen P. et al., 2020, Nature Methods, 17, 261

APPENDIX: ADDITIONAL FIGURES

Wagg T., Breivik K., de Mink S. E., 2022, ApJS, 260, 52

Corner plots of the sampled posterior distributions for each of the analyses discussed are found on this and the following pages: Fig. A1 for the LMC in isolation with LISA instrumental noise, and Fig. A2 (Fig. A3) for the spectral (spatial) parameters of the analysis with the LMC + MW + LISA instrumental noise.

van der Marel R. P., Alves D. R., Hardy E., Suntzeff N. B., 2002, AJ, 124,

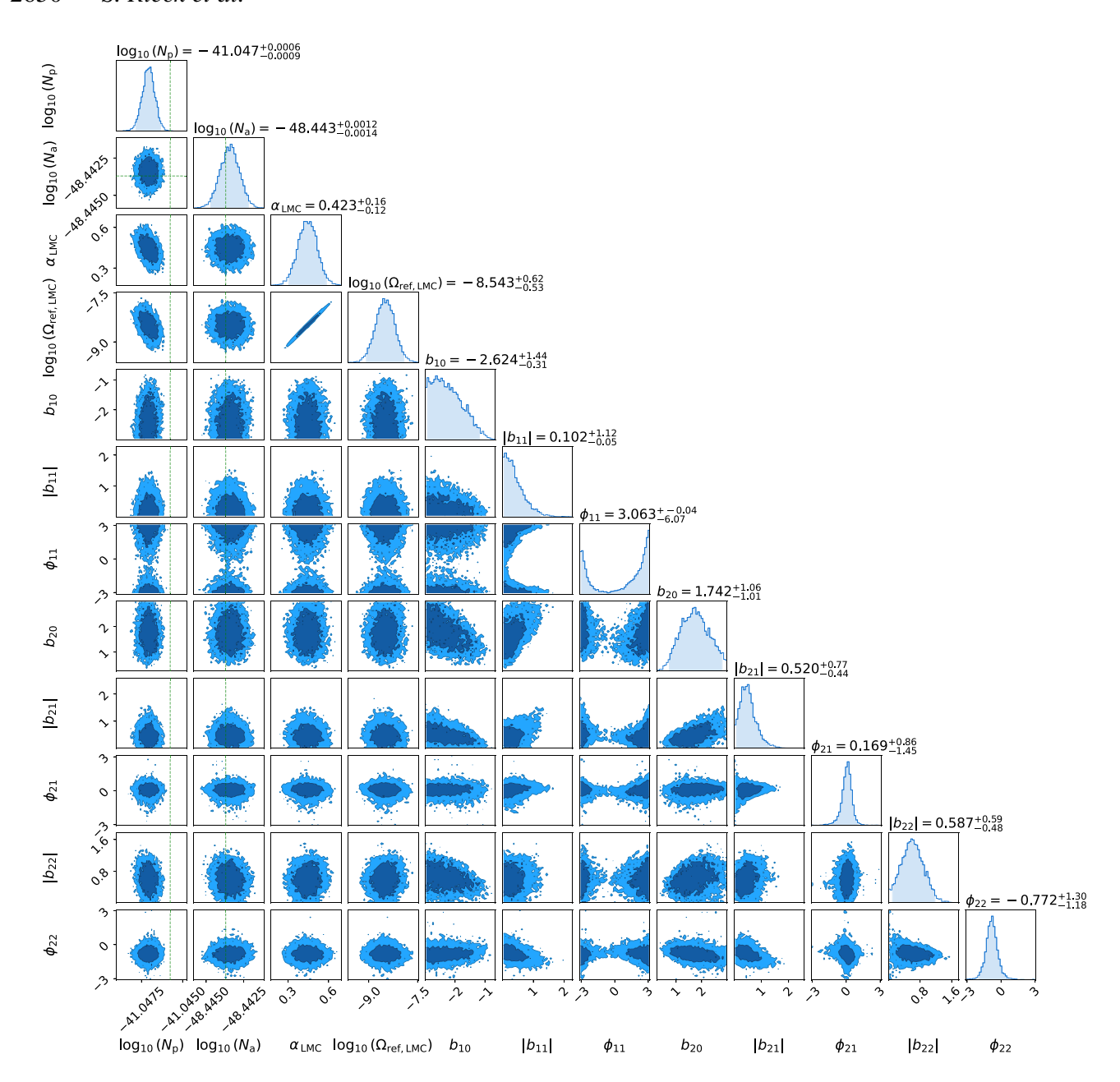


Figure A1. Corner plot for the analysis in Section 3.2 of the LMC SGWB in isolation, showing the one- and two-dimensional marginalized posterior samples for each of our model parameters. These are (moving left to right): the LISA position and acceleration noise amplitudes $(\log_{10}(N_p))$ and $\log_{10}(N_p)$, respectively); the SGWB power-law model slope (α) and \log amplitude $(\log_{10}(\Omega_{ref}))$; and the magnitude and phase of the $b_{\ell m}$ spherical harmonic coefficients up to $\ell_{max}^b = 2$ $(\ell_{max}^a = 4)$. The true values of the noise parameters are marked with green dashed lines. The remaining parameters do not have defined true values, as our simulated signal is generated from a DWD population. Contours shown are 1σ and 2σ . A careful eye will note a slight bias in the recovery of the position noise contribution, N_p . This is a result of our power-law spectral model being an imperfect fit for the population-derived, non-power-law spectrum of the LMC SGWB; repeating this study without the inclusion of the LMC signal results in unbiased noise recoveries. Potential future approaches to fitting the LMC signal with higher fidelity are discussed in Section 4.

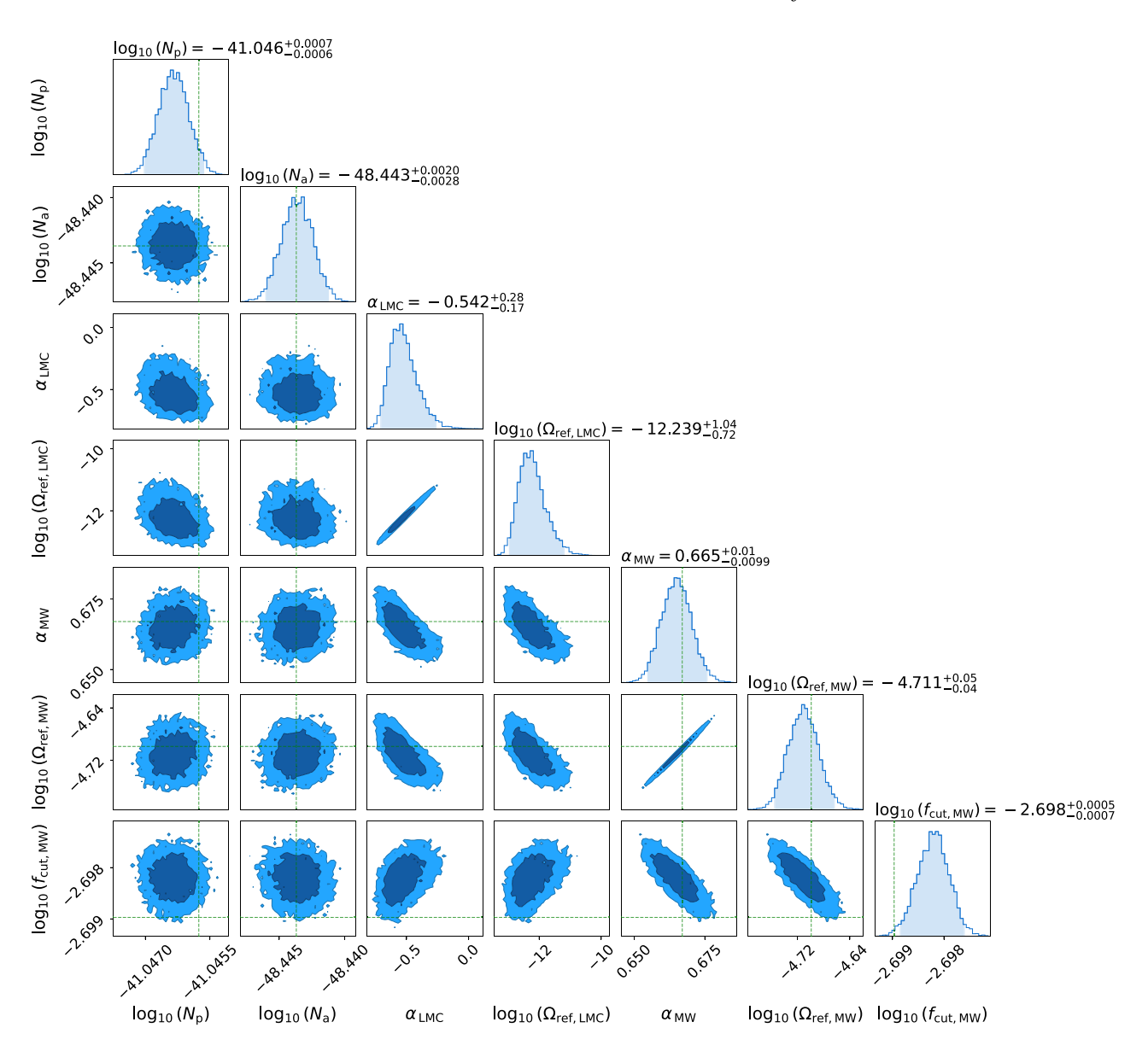


Figure A2. Spectral parameters corner plot for the analysis in Section 3.3 of the LMC SGWB alongside a simple simulation of the MW foreground, showing the one- and two-dimensional marginalized posterior samples for all spectral model parameters. Spatial parameter samples are shown in Fig. A3. Included parameters are (moving left to right): the LISA position and acceleration noise amplitudes $(\log_{10}(N_p)$ and $\log_{10}(N_a)$, respectively); the LMC SGWB power-law model slope (α_{LMC}) and log amplitude $(\log_{10}(\Omega_{ref,LMC}))$; and the MW foreground truncated power-law model slope (α_{MW}) , log amplitude $(\log_{10}(\Omega_{ref,LMC}))$, and log cutoff frequency $(\log_{10}(f_{cut,MW}))$. True values are marked with green dashed lines. As before, the LMC model parameters do not have defined true values. Contours shown are 1σ and 2σ .

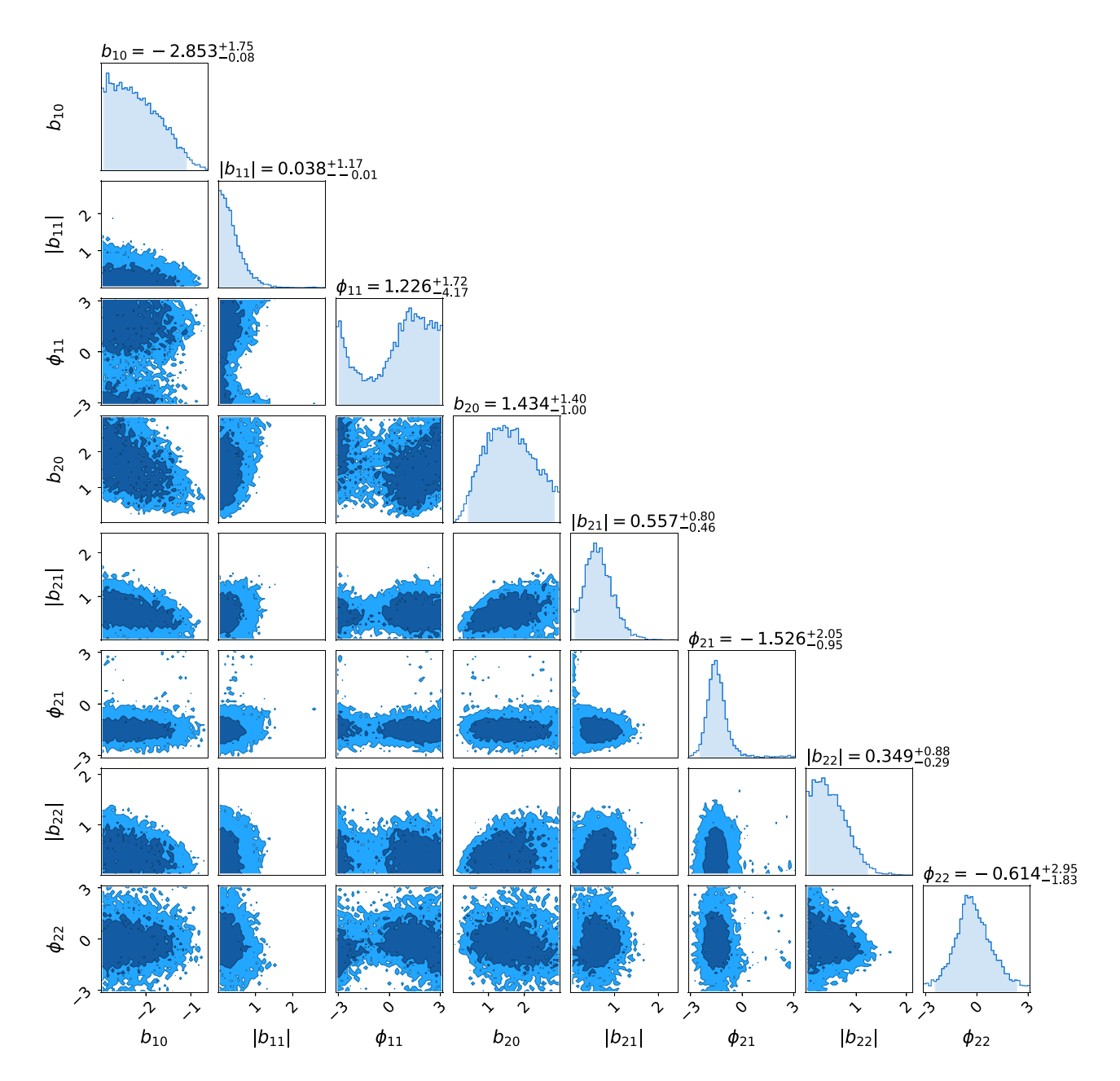


Figure A3. Spatial parameters corner plot for the analysis in Section 3.3 of the LMC SGWB alongside a simple simulation of the MW foreground, showing the one- and two-dimensional marginalized posterior samples for the LMC spatial model parameters (the MW spatial model is fixed; see Section 3.3). Parameters shown are the magnitude and phase of the $b_{\ell m}$ spherical harmonic coefficients up to $\ell_{\rm max}^b = 2$ ($\ell_{\rm max}^a = 4$). Contours shown are 1σ and 2σ .

This paper has been typeset from a TEX/IATEX file prepared by the author.